Geochimica et Cosmochimica Acta 420 (2026) 246–259

Contents lists available at ScienceDirect

Geochimica et Cosmochimica Acta

journal homepage: www.elsevier.com/locate/gca

Non–equilibrium K isotope fractionation during alunite precipitation from hydrothermal fluids and the implications

Yuqi Li, Yang Zhang, Xudong Che, Zhimin Tang, Weiqiang Li *

State Key Laboratory of Critical Earth Material Cycling and Mineral Deposits, School of Earth Sciences and Engineering, Nanjing University, Nanjing, Jiangsu, China

ARTICLE INFO

Associate editor: Fang-Zhen Teng

Keywords:
Alunite
Natroalunite
K isotopes
Isotope fractionation
Kinetic effects
Hydrothermal experiment

ABSTRACT

Alunite and alunite–group minerals occur in diverse terrestrial environments as well as on the Martian surface. The K isotope ratios of alunite and its solid–solution series could be used to trace relevant high– and low–temperature processes on Earth and Mars. However, such applications are limited by the lack of detailed understanding of K isotope fractionation behaviors and their controlling factors during alunite precipitation. In this study, we experimentally synthesized alunite and natroalunite under various hydrothermal conditions, and measured the apparent K isotope fractionation factors between alunite and aqueous fluids ($\Delta^{41}K_{alu-aq}$) under different conditions including variable temperature, reaction time, solution chemistry, and pH of aqueous fluids. Specifically, at 188°C, the $\Delta^{41}K_{alu-aq}$ increased from –0.39 ± 0.09‰ to 0.30 ± 0.03‰ in 210 days, indicating continuous exchange of K isotopes between alunite and aqueous solution throughout the experiments. Given constant reaction temperature (188°C) and reaction time (1 day), when the solution pH increased from 1.10 to 1.66, there was a systematic decrease in the size of synthesized alunite, while the $\Delta^{41}K_{alu-aq}$ increased from 0.02 ± 0.09‰ to 0.31 ± 0.05‰; and when K/(K + Na) of synthesized alunite decreased from 0.99 to 0.68, the $\Delta^{41}K_{alu-aq}$ increased from –0.10 ± 0.10‰ to 0.40 ± 0.11‰. Regardless of experimental conditions, the measured $\Delta^{41}K_{alu-aq}$ values are drastically lower than the theoretically predicted $\Delta^{41}K_{alu-aq}$ values at equilibrium, implying that the precipitation of alunite should be dominated by kinetic effects for K isotopes. Nonetheless, the experimentally obtained $\Delta^{41}K_{alu-aq}$ in our study are more consistent with the inferred K isotope fractionation between natural alunite and hydrothermal fluids. This implies that K in natural alunite may not reach isotopic equilibrium with hydrothermal fluids during alunite formation processes, thus experimentally determined K isotope fractionation factors are crucial for interpreting K isotope data of alunite and alunite–group minerals in nature.

1. Introduction

Alunite [$KAl_3(SO_4)_2(OH)_6$] is a common mineral stable over a wide temperature range (from ambient conditions to 500°C) and can occur in high–sulfidation hydrothermal deposits and related magmatic–hydrothermal systems (Rye et al., 1992; Rye, 2005). Alunite could be used to study hydrothermal fluid evolution and metallogenesis (Quang et al., 2005; Bissig and Riquelme, 2010; Perello et al., 2020). For example, ^{40}K–^{40}Ar and ^{40}Ar–^{39}Ar dating of alunite provided constraints on the magmatic and hydrothermal histories of porphyry ore–forming systems (Mederer et al., 2019; Hedenquist et al., 2020; Sahlstrom et al., 2020; Duan et al., 2022), and as vectors to the mineralization center in ore fields (Zhou et al., 2022; Sun et al., 2023). As a typical sulfate–bearing hydrothermal alteration product, alunite has also been used to constrain the pH and temperature of hydrothermal fluids (Coward et al., 2023; Hedenquist and Arribas, 2022; Li et al., 2020b; Manalo et al., 2022). Moreover, alunite–group minerals (e.g., alunite and jarosite) have been identified on the Martian surface (Ehlmann et al., 2016; Martin et al., 2017; Rampe et al., 2020), which potentially hold crucial information of water–rock interaction and weathering histories on Mars.

Potassium (K) constitutes a key component in alunite, and theoretical calculations predicted significant K isotope fractionation between alunite and aqueous solutions ($\Delta^{41}K_{alu-aq}$), which can exceed 1‰ even at hydrothermal ore–forming temperatures (e.g., 400°C) (Li et al., 2019b). This implies that K isotopes in alunite and its solid–solution series have great potential to trace the epithermal and supergene processes. However, the K isotope fractionation behavior during alunite precipitation from aqueous solutions has not been experimentally investigated. In addition, alunite belongs to the alunite supergroup, which comprises over 50 mineral species (Mills et al., 2009; Bayliss et al., 2010). The

* Corresponding author.
E-mail address: liweiqiang@nju.edu.cn (W. Li).

https://doi.org/10.1016/j.gca.2026.03.040
Received 9 November 2025; Accepted 23 March 2026
Available online 2 April 2026

general formula of this supergroup is $DG_3(TO_4)_2(OH, H_2O)_6$, where the D sites contain cations such as K and Na, G sites typically contain Al and Fe, and T sites are dominated by S and P (Parker, 1962; Stoffregen and Cygan, 1990; Stoffregen, 1993; Stoffregen et al., 1994a, 1994b; Stoffregen et al., 2000). The substitution of K by Na in alunite is common in nature, and complete solid solutions of alunite-natroalunite can be formed (Fielding, 1980; Stoffregen and Cygan, 1990; Rudolph and Mason, 2001). However, the isotopic effects associated with D sites cation substitution in alunite remain unconstrained. These knowledge gaps restricted the application of K isotopes in isotopic tracing studies of alunite for various terrestrial and Martian samples.

In this study, alunite and its K-Na solid solution series were synthesized under various experimental conditions, including temperature, solution pH, initial K/Na ratios, and reaction time. The K isotope fractionation factors between alunite and aqueous fluids were measured, providing key experimental constraints on K isotope fractionation behaviors during alunite precipitation. In addition, natural alunite samples from two hydrothermal ore deposits were measured for K isotopes, and the K isotope compositions of the alunite samples were interpreted based on experimental results, with implications for extending the K isotope system to trace a wide range of processes on Earth and Martian surface using alunite–natroalunite records.

2. Experiments, samples, and analyses

2.1. Mineral synthesis experiments

Alunite samples were synthesized under both low–temperature (98°C, 150°C, and 188°C) and high–temperature (400°C) conditions. Low–temperature alunite was directly synthesized by mixing and heating aqueous solutions containing K^+, Al^{3+}, and SO_4^{2-}. By contrast, high–temperature alunite (400°C) was synthesized via replacement of natroalunite in a K–rich solution. For alunite synthesis, different stock solutions, including K_2SO_4 (0.48 M), KOH (0.95 M), Na_2SO_4 (0.48 M), and $Al_2(SO_4)_3$ (0.24 M) were prepared by dissolving reagent–grade salts of K_2SO_4, KOH, Na_2SO_4, and $Al_2(SO_4)_3{\cdot}16H_2O$ in deionized water. For all experiments, the initial molar ratios of (K + Na)/Al in aqueous solutions were set to 2:1 to ensure that K (and Na) remained in excess in aqueous solutions after alunite precipitation, maintaining a fluid–solid K mass balance favorable for K isotopic investigation.

2.1.1. Low temperature alunite synthesis experiments

For the low–temperature experiments, four series of experiments were conducted, including the time series, pH series, temperature series, and K–Na series. For the time series experiments, 3.5 mL of $Al_2(SO_4)_3$ stock solution, 3.5 mL of K_2SO_4 stock solution, and 1 mL of deionized water were mixed in a 10 mL Teflon–lined hydrothermal bomb. The bombs were then sealed and placed in an oven with a preheated oven at 188°C for variable reaction time ranging from 12 h to 210 days. All experiments were run in duplicate. Given the rapid precipitation of alunite under our experimental conditions, additional short–duration experiments were conducted and sampled at high temporal resolution to quantity the mass of precipitated alunite within the first 24 h.

For the pH series experiments, 3.5 mL of $Al_2(SO_4)_3$ stock solution and 1 mL of deionized water were initially mixed with 1 mL of deionized water. K_2SO_4 and KOH stock solutions were then added at varying ratios to adjust the pH of the initial aqueous solutions (Table 1). The resulting mixtures were sealed in Teflon–lined hydrothermal bombs and heated at 188°C for 24 h.

For the temperature series experiments, 3.5 mL of $Al_2(SO_4)_3$ stock solution, 3.5 mL of K_2SO_4 stock solution, and 1 mL of deionized water were mixed (Table 1). Then the mixtures were sealed in hydrothermal bombs and heated at 188°C, 150°C, or at 98°C for 24 h at each temperature.

Table 1
Summary of alunite synthesis experiments.

Tempe −rature	Reaction vessel	Starting material				Experimental duration
Time/Temperature series experiments						
400°C	Gold capsule	0.15 mL ample K_2SO_4 suspension + fine grained synthesized natroalunite (d ≤ 20 μm)				1, 4 and 8 days
188°C	Teflon liner of bomb	3.5 mL $Al_2(SO_4)_3$ stock solution + 3.5 mL K_2SO_4 stock solution + 1 mL deionized water				0.5, 0.75, 1, 2, 4, 8, 16, 64 128 and 210 days
150°C	Teflon liner of bomb	3.5 mL $Al_2(SO_4)_3$ stock solution + 3.5 mL K_2SO_4 stock solution + 1 mL deionized water				1 day
98°C	Teflon liner of bomb	3.5 mL $Al_2(SO_4)_3$ stock solution + 3.5 mL K_2SO_4 stock solution + 1 mL deionized water				1 day
pH series experiments						
		$Al_2(SO_4)_3$ stock solution	K_2SO_4 stock solution	KOH stock solution	Deionized water	
188°C	Teflon liner of bomb	3.5 mL	3.5 mL	0 mL	1 mL	1 day
			3 mL	0.5 mL		
			2.5 mL	1 mL		
			2 mL	1.5 mL		
			1.5 mL	2 mL		
			1 mL	2.5 mL		
			0.5 mL	3 mL		
			0 mL	3.5 mL		
K-Na series experiments						
		$Al_2(SO_4)_3$ stock solution	K_2SO_4 stock solution	Na_2SO_4 stock solution	Deionized water	
188°C	Teflon liner of bomb	3.5 mL	0 mL	3.5 mL	1 mL	1 day
			0.05 mL	3.45 mL		
			0.1 mL	3.4 mL		
			0.15 mL	3.35 mL		
			0.2 mL	3.3 mL		
			0.25 mL	3.25 mL		
			0.3 mL	3.2 mL		
			0.35 mL	3.15 mL		
			0.4 mL	3.1 mL		
			0.45 mL	3.05 mL		
			0.5 mL	3 mL		
			1 mL	2.5 mL		
			1.5 mL	2 mL		
			2 mL	1.5 mL		
			2.5 mL	1 mL		
			3 mL	0.5 mL		
			3.5 mL	0 mL		

For the K–Na series experiments, 3.5 mL of $Al_2(SO_4)_3$ stock solution and 1 mL of deionized water were first mixed. Then, the stock solutions of K_2SO_4 and Na_2SO_4 were added at varying proportions to obtain different K/Na ratios in the initial aqueous solutions mixtures (Table 1). The resulting mixture solutions were sealed in hydrothermal bombs and heated at 188°C for 24 h.

After the reactions, the hydrothermal bombs were air–quenched to room temperature. The supernatant was collected using a pipette. The solid products were separated by centrifugation, washed three times with deionized water, and dried in an oven at 50°C for 12 h.

2.1.2. High temperature alunite synthesis experiments

For high temperature experiments, alunite was synthesized by reacting fine–grained natroalunite with K–bearing aqueous solutions in a gold capsule placed in Rapid–quench cold–seal vessels at 400°C and 1000 bar. The fine–grained natroalunite was prepared by heating a mixture of 0.2 M Na_2SO_4 solution and 0.1 M $Al_2(SO_4)_3$ dilute solution in a centrifuge tube at 50°C for 22 h. The synthesized natroalunite crystals were then separated by centrifugation, washed three times with deionized water, and dried at 50°C for 12 h. For each experiment, 0.112 mL of K_2SO_4 solution (6.34×10^{-1} mol/L), 0.038 mL of 30% H_2SO_4 (w/w%), and 10 mg of fine–grained synthesized natroalunite were loaded and sealed in a gold capsule (3 cm long, 4.7 mm inner diameter). Temperature was measured and controlled using a Eurotherm controller with an Inconel 600 thermocouple with an accuracy of ± 5°C. Water served as the pressure medium for the reaction vessel, and the pressure was monitored by a pressure gauge with an accuracy of ± 40 bar.

After heating for 1, 4, and 8 days, the capsules were quenched to room temperature and dried at 50°C for 12 h. The capsules were checked for leakage by comparing the weights before and after the reactions. Then, the capsules were opened, and the reaction products were transferred to clean centrifuge tubes and separated via centrifugation. The reacted solid products were washed three times with deionized water and air–dried prior to analysis.

2.2. Natural alunite samples

The Anhui–Fanshan alunite deposit in Anhui province of China is characterized by Cretaceous volcanic–subvolcanic sequences with multistage magmatism (Fan et al., 2010; Tang, 2008; Zhang, 2011). The ore–hosting rocks predominantly comprise trachyandesites and tuffs of the Cretaceous Zhuanqiao Formation, which host an extensive lithocap formed through magmatic–hydrothermal fluid–rock interactions. This lithocap represents a key component of the continental volcanic metallogenic system in the Middle–Lower Yangtze River region. Dominant mineral assemblages with the lithocap include quartz–silica, vuggy quartz–alunite–pyrite, quartz–dickite–kaolinite ± alunite, and kaolinite–interstratified illite and smectite. The age of hydrothermal alunite was 131 ± 6 Ma based on $^{40}Ar/^{39}Ar$ dating (Li et al., 2019). The alunite was formed at temperature range of 260 to 290°C (Fan et al., 2010). Alunite from Anhui–Fanshan occurs as euhedral to subhedral grains, exhibiting diverse aggregate morphologies, including radial, fibrous, and bladed forms, which fill open spaces or pores within quartz. Alunite is commonly associated with vuggy to massive quartz, granular or disseminated hematite, pyrite, and minor rutile, reflecting typical hydrothermal alteration characteristics. The alunite is red to light purple in color, with no obvious evidence of supergene weathering. Quartz cementation is prominent, and hematitization is observed in localized areas.

The Cangnan–Fanshan alunite deposit in Zhejiang province of China is hosted in the late Cretaceous Chaochuan Formation, comprising tuffaceous clastics and breccias. $^{40}Ar/^{39}Ar$ dating of alunite yielded an age of 74.5 ± 1.49 Ma (Ren et al., 1998). Fluid inclusion microthermometry (175–300°C) (Wang et al., 1997) and sulfur isotopic data ($\delta^{34}S = 13.6‰–16.0‰$; He et al., 2009) indicate that the mineralization originated from an acidic fluid system involving mixing of magmatic-hydrothermal fluids with meteoric water. Alunite from the Cangnan–Fanshan deposit occurs as euhedral to subhedral, fine– to coarse–grained crystals. Alunite aggregates mainly display vein–like and disseminated morphologies, filling open pore systems within the volcanic rock matrix or forming intergrowth associations with quartz. Alunite crystals commonly show pale-red to light purple hues, while the associated quartz typically exhibits porous to cryptocrystalline characteristics. The primary paragenetic minerals include kaolinite, dickite, and pyrophyllite, accompanied by disseminated star–like hematite and localized hematitized bands.

A total of 29 alunite–bearing samples were collected, of which 17 were from the Anhui–Fanshan (Dafanshan area) in Anhui Province and 12 from the Cangnan–Fanshan deposit in Zhejiang Province (Fig. S2 and S3). The samples were crushed into sub–mm sized fragments, and alunite grains were handpicked using binocular microscopes and ground to a fine powder with an agate pestle and mortar for K isotope analysis.

2.3. Analytical methods

2.3.1. Characterization of minerals and aqueous solutions

Powder X–ray diffraction (XRD) analysis of the solid experimental products and natural samples was performed using a Rigaku Rapid II dual–source X–ray diffractometer (XRD) at the State Key Laboratory of Critical Earth Material Cycling and Mineral Deposits, Nanjing University. The instrument was equipped with a rotating anode Mo target X–ray source (Mo $K_\alpha = 0.71073$ Å) and operating at 50 kV and 90 mA. Diffraction patterns were acquired after an exposure time of 9 min. Mineral identification and data processing were performed using Jade 6.5 and Fullprof software.

Solid products from each alunite were imaged for morphology using scanning electron microscopy (SEM). The SEM images were used to measure the average cross–sectional area and form factor with the Particles and Cracks Analysis System (PCAS) software (Liu et al., 2011). The average cross–sectional area indicates the average particle size of the granular crystals. The form factor (ff) quantifies the proximity between irregular particles and spherical particles, which is defined by perimeter (C) and area (S) as $ff = 4 \times \pi \times S/C^2$ (Liu et al., 2011). For example, a crystal section corresponds to a perfect circle when ff = 1 and a square when ff = 0.785. The roundness and complexity of crystal section boundary increase with decreasing ff.

Potassium concentrations in aqueous solutions were determined using a flame photometer, calibrated with a series of gravimetrically prepared K standard solutions (0 to 10 ppm). The analytical uncertainty for elemental concentration measurement was better than ± 5% (RSD). The concentration of Al in the residual solutions was measured by inductively coupled plasma–optical emission spectrometer (ICP–OES) (Skyray ICP 3000), with analytical precision better than ± 5%.

Solution pH was measured at room temperature using a temperature–corrected pH/ion/mV meter equipped with an Ag/AgCl pH probe. The meter was calibrated with AQUASPEX standard pH buffer solutions, and the probe precision was ~ 0.1 pH unit.

2.3.2. K isotope analysis

The solid experimental products and natural alunite samples were dissolved in *aqua regia*. Based on previously determined K concentration data, a small portion of the dissolved sample containing ~ 100 μg K was evaporated to dryness at 96°C. The solid residue was redissolved in 0.5 mL of 0.2 M HNO_3 + 0.05 M HF for subsequent ion–exchange chromatography. The separation procedure followed the ion exchange protocol described by Li et al. (2016). Each column contained 0.4 mL of 100–200 mesh BioRad® AG50W–x8 resin. Samples were loaded onto the column using 500 μL of 0.2 M HNO_3 + 0.05 M HF. Matrix interferences were removed via sequential elution: first with 5 mL of 0.2 M HNO_3 + 0.05 M HF to elute Al^{3+} and SO_4^{2-}, followed by 1.5 mL of 1.5 M HNO_3 to elute Na^+. Potassium was subsequently recovered with 9 mL of 0.5 M HNO_3. Finally, the column was washed with 2 mL of 6 M HCl to remove

the residual matrix components. The recovery of K was 99.9 ± 0.4% (2SD, n = 77).

The K isotope ratios were measured using a Nu 1700 Sapphire multi–collector inductively coupled plasma mass spectrometer (MC–ICP–MS) at Nanjing University. The instrument was operated under high–energy, high mass resolution, dry plasma mode. Each isotopic analysis consisted of 40 cycles of 5 s integration time, yielding an internal precision better than 0.04‰ (2 relative standard error) for $^{41}K/^{39}K$ ratios. All K isotope data were measured using a standard–sample–standard bracketing method, with concentration matching between samples and bracketing standard better than ± 5% at 3 ppm. The long–term external reproducibility of K isotope analysis was better than ± 0.07‰ in $^{41}K/^{39}K$ (N = 120, 2 standard deviations), based on repeated analyses of multiple NIST SRM 3141a against in–house A–K standard, as well as purified USGS rock standards (An et al., 2022).

The K isotope data are reported in the standard δ–notation as per mil (‰) deviations relative to the international K isotope standard NIST SRM 3141a:

$$\delta^{41}K = [\frac{(^{41}K/^{39}K)_{sample}}{(^{41}K/^{39}K)_{standard}} - 1] \times 100 \quad (1)$$

For the experiments, fractionation in K isotopes between the solid and aqueous phase is expressed as:

$$\Delta^{41}K_{du-aq} = \delta^{41}K_{alu} - \delta^{41}K_{aq} \quad (2)$$

The error in K isotope fractionation is calculated via error propagation function:

$$Err\Delta^{41}K_{alu-aq} = [(Err\delta^{41}K_{alu})^2 + (Err\delta^{41}K_{aq})^2]^{1/2} \quad (3)$$

where $Err\Delta^{41}K_{alu-aq}$ is the error of the K isotope fractionation, and $Err\delta^{41}K_{alu}$ and $Err\delta^{41}K_{aq}$ are the analytical uncertainty (2σ) for solid phase alunite and aqueous solution, respectively.

3. Results

3.1. Mineralogy of alunite synthesis experimental products

Both SEM and XRD results confirmed the successful synthesis of pure alunite in all the time series (Fig. 1) and pH series (Fig. 2) experiments. In time series experiments, the mass of solid products increased rapidly within the first 4 h of reaction then remained relatively constant with prolonged reaction time (Fig. 1h). During the initial stage of the reaction, spherical alunite grains were precipitated (Fig. 1a). As the reaction progressed, the spherical alunite grains started to exhibit anhedral to subhedral textures (Fig. 1b–g). The solution pH also exerted significant effects on the morphology of alunite. Under lower pH conditions (pH = 1.10–1.36), the alunite grains exhibited well–developed idiomorphic form (Fig. 2a–d). However, as the solution pH increased, the crystals became less euhedral, and their grain size decreased at the same reaction time (Fig. 2e–g). PCAS analyses of the SEM images showed that as pH increased from 1.10 to 1.66, the average grain cross sectional area of alunite decreased from 2170 μm^2 to 410 μm^2, and the average form factor increased from 0.67 to 0.85. There is a negative correlation between pH and the average particle size (Fig. 3b) and a positive correlation between pH and the crystal roundness (or form factor, Fig. 3c). For high–temperature experiments, K–alunite was synthesized by reacting Na–alunite with K–bearing fluids. The initial natroalunite display a distinct thin and long rod–shaped morphology (Fig. 2h). The SEM and XRD results verified the complete replacement of Na–alunite by K–alunite at 400°C (Fig. S1).

The unit–cell parameter *c* of alunite calculated based on XRD spectrum is an indicator for substitutions in the D sites, as it directly reflects structural variations along [0 0 1] direction (Stoffregen et al., 2000). In K–Na series synthesis experiments conducted at 188°C, the *c* parameter of alunite synthesized after 1 day ranged from 16.88 Å to 17.12 Å, corresponding to a solid–phase K/(K + Na) ratio of 0.49 to 1.00 (Fig. 6b, Table S3). Notably, across all mineral synthesis experiments (regardless of reaction time and temperature), a consistent linear correlation was observed between the solid K/(K + Na) ratio and the *c* parameter of alunite.

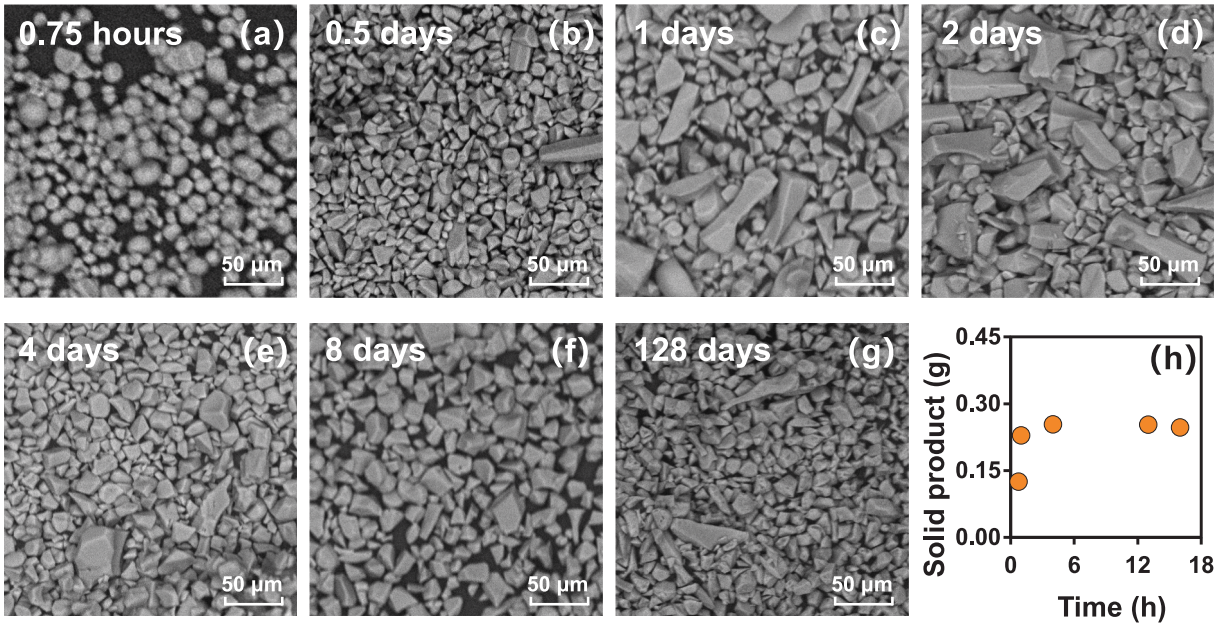

Fig. 1. (a–g) Secondary electron images (SEI) of solid products synthesized with different reaction time. (h) Mass of alunite solid product synthesized over 0.75–16 h at 188°C.

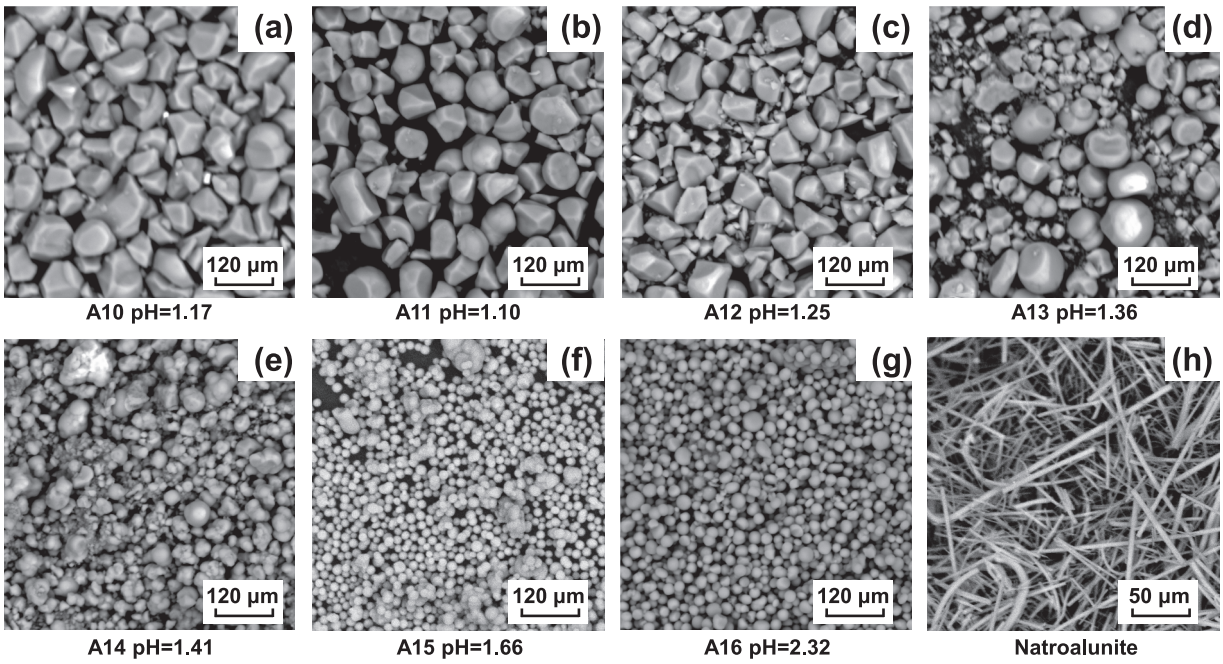

Fig. 2. (a–g) Secondary electron images (SEI) of alunite solid products synthesized at 188°C under different pH conditions. The pH values refer to the residual solution at room temperature after reaction. (h) Secondary electron images of Na-alunite synthesized at pH = 1.17. (See sample ID in Table S2.).

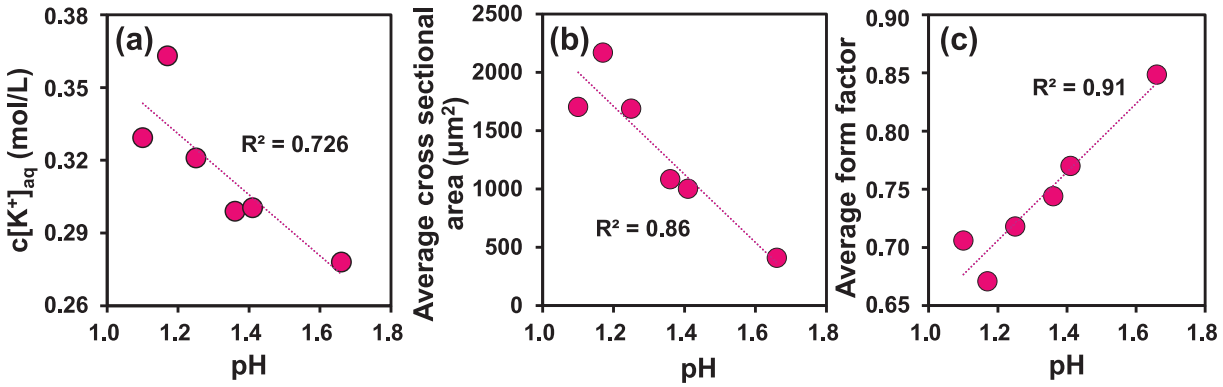

Fig. 3. Effect of solution pH on the solution chemistry and morphology of products (a) The K concentration of residual solution with the temperature of 188°C and 1 day reaction. (b) Average cross-sectional area calculated by PCAS based on the SEM images. (c) Average form factor calculated by PCAS based on the SEM images. The pH refers to the residual solution after reaction at room temperature.

3.2. Potassium isotope results of alunite synthesis experiments

The K isotope compositions of the synthesized alunite and aqueous solutions varied with reaction time, solution pH, and temperature in the experiments. In most experiments, aqueous fluids dominated the mass of K over alunite, thus their $\delta^{41}K_{aq}$ values changed little due to isotope mass balance, and the measured apparent K isotope fractionation factors between alunite and aqueous solutions ($\Delta^{41}K_{alu-aq}$) were mainly controlled by the changes in $\delta^{41}K$ values of alunite. For concision, $\Delta^{41}K_{alu-aq}$ values are used to summarize the results of some experiments. In addition, the $\delta^{41}K$ values of natural alunite samples also show considerable variabilities. All raw isotope data for the different phases are provided in Supplementary Material (Table S1, S2 and S3).

3.2.1. Time series alunite synthesis experiments

At the beginning of the time-series experiments at 188°C, the synthesized alunite had $\delta^{41}K$ values lower than those of the aqueous solutions (i.e., $\delta^{41}K_{aq} = 0.34 \pm 0.06$‰ for the starting stock K_2SO_4). As the reaction progressed, the alunite became isotopically heavier, with $\delta^{41}K_{alu}$ increased from –0.03 ± 0.07‰ to 0.54 ± 0.03‰ (Fig. 5a). Correspondingly, the $\Delta^{41}K_{alu-aq}$ fractionation between synthesized alunite and aqueous solution increased from –0.39 ± 0.09‰ after 12 hours to 0.30 ± 0.03‰ after 210 days (Fig. 5c). Results from duplicate experiments (A02 and ATS04–1; A03 and ATS05–1) were almost identical (see Table S1).

For high temperature experiments at 400°C, the $\delta^{41}K$ values of alunite ranged from 0.36 ± 0.04‰ to 0.43 ± 0.04‰. The $\delta^{41}K$ of aqueous solutions remained stable at 0.27‰ from 1 day to 4 days, then increased to 0.31 ± 0.04‰ after 8 days (Fig. 5b), and the measured $\Delta^{41}K_{alu-aq}$ decreased from 0.16 ± 0.05‰ to 0.09 ± 0.08‰ in the first 4 days and stabilized after 8 days (Fig. 5d).

3.2.2. pH series experiments

In the pH–series experiments performed at 188°C for 1 day, K isotope fractionation factors showed a strong correlation with the pH of the aqueous solution (Fig. 4; Table S2). It should be noted that the initial reactant solutions were prepared by mixing K_2SO_4 and KOH at various proportions, with $\delta^{41}K$ values of 0.33 ± 0.05‰ and 0.05 ± 0.05‰,

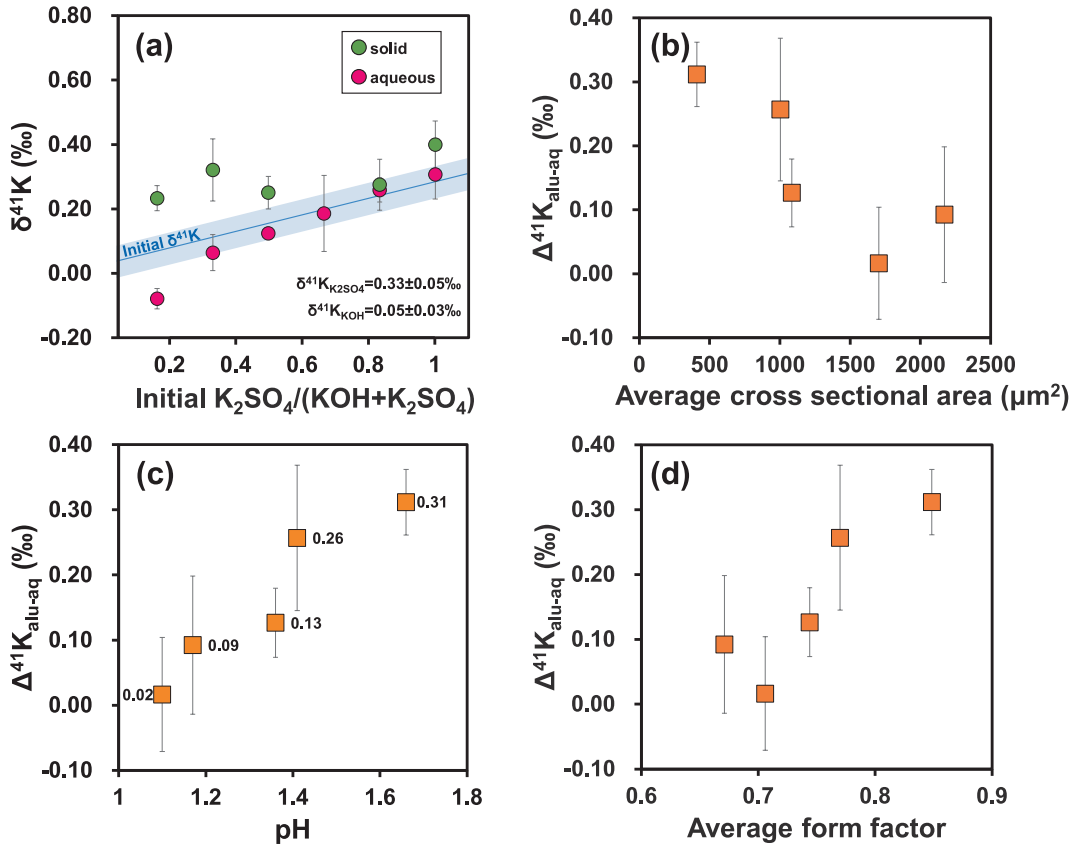

Fig. 4. The potassium isotope data for pH-controlled experiments. (a) The $\delta^{41}K$ values of alunite and coexisting aqueous solutions after reaction. (b) The average cross-sectional area versus the $\Delta^{41}K_{alu\text{-}aq}$ values. (c) The $\Delta^{41}K_{alu\text{-}aq}$ values (numerically labeled in ‰) with the final pH conditions. (d) The relationship between the average form factor and the $\Delta^{41}K_{alu\text{-}aq}$ values.

respectively. Consequently, the initial aqueous solutions exhibited variable $\delta^{41}K$ values proportional to $K_2SO_4/(K_2SO_4 + KOH)$ molar ratio (Fig. 4a). After reactions, the $\delta^{41}K_{aq}$ varied from 0.02 ± 0.06‰ to 0.31 ± 0.08‰ with corresponding $\delta^{41}K_{alu}$ varying from 0.40 ± 0.07‰ to 0.23 ± 0.04‰. Correspondingly, the $\Delta^{41}K_{alu\text{–}aq}$ fractionation factors varied from 0.02 ± 0.09‰ at pH 1.10 to 0.31 ± 0.05‰ at pH 1.66 (Fig. 4c). A strong correlation was also observed between $\Delta^{41}K_{alu\text{–}aq}$ and the cross–section area of synthesized alunite grains (Fig. 4b, d).

3.2.3. K–Na series and temperature series experiments

The measured K isotope fractionation factors ($\Delta^{41}K_{alu\text{–}aq}$) exhibited significant variation depending on the K/Na ratio of the (natro–)alunite (Fig. 6). In experiments conducted at 188°C for 1 day, the $\delta^{41}K_{aq}$ varied from 0.08 ± 0.10‰ to 0.45 ± 0.04‰, with corresponding $\delta^{41}K_{alu}$ values ranging from 0.47 ± 0.04‰ to 0.35 ± 0.09‰ (Table S3). The $\Delta^{41}K_{alu\text{–}aq}$ values decreased from 0.40 ± 0.11‰ to –0.10 ± 0.10‰ as the K/(K + Na) ratios increased from 0.68 to 0.99 (Fig. 6a).

Experiments performed at 150°C for 1 day yielded a $\delta^{41}K_{aq}$ value of 0.37 ± 0.06‰ and 0.60 ± 0.09‰ for $\delta^{41}K_{alu}$, resulting in a $\Delta^{41}K_{alu\text{–}aq}$ value of 0.23 ± 0.11‰. In contrast, at a lower temperature of 98°C over the same duration, the aqueous phase had a $\delta^{41}K_{aq}$ of 0.34 ± 0.08‰, while alunite showed a heavier isotopic composition of 0.62 ± 0.10‰, yielding a similar fractionation of 0.28 ± 0.13‰ (Table S3).

3.3. The K isotope compositions of natural alunite

The alunite samples from Anhui–Fanshan alunite deposit have K/(K + Na) ratios ranging from 0.67 to 0.95, and $\delta^{41}K$ values varying from –0.83 ± 0.01‰ to –0.02 ± 0.07‰. For the Cangnan–Fanshan deposit, the alunite samples have K/(K + Na) ratios ranging from 0.58 to 0.96 and $\delta^{41}K$ values ranging from –0.65 ± 0.04‰ to 0.21 ± 0.03‰ (Fig. 7a), but there is no obvious correlation between $\delta^{41}K$ and K/(K + Na) ratios.

4. Discussion

4.1. The nucleation and growth of alunite

Solution pH exerts strong control on the size and morphology of synthesized alunite (Fig. 2a–g). Under relatively higher pH conditions (pH = 1.66, 2.32), alunite crystals are finer–grained (smaller cross–section areas; Fig. 3b) and less euhedral (form factor closer to 1; Fig. 3c). Meanwhile, the K^+ concentration of the remaining aqueous solution was lower in higher pH experiments (Fig. 3a), indicating larger mass of aqueous K was incorporated into alunite precipitates than lower pH experiments. Together, these suggest that more alunite grains were precipitated under higher pH conditions. Based on the K concentration and cross section area data (Fig. 3a–b), and assuming a simplified uniform spherical geometry for all alunite crystals, we estimate that 1.85×10^6 alunite grains formed in the pH = 1.17 experiment, compared to an estimation of 2.19×10^7 alunite grains in the pH = 2.32 experiment, a difference in one order of magnitude (Table S4). Therefore, nucleation rate of alunite is greater under higher pH conditions than lower pH conditions.

Considering the chemical formula of alunite precipitation:

$$K^+ + 3Al^{3+} + 2SO_4^{2-} + 6H_2O = KAl_3(SO_4)_2(OH)_6 + 6H^+ \quad (4)$$

alunite precipitation is a H^+ releasing process, which means that lower pH is thermodynamically unfavorable for alunite precipitation. This may contribute to the significantly higher nucleation rate of alunite in higher pH experiments. According to LaMer's classic model for particle formation (Lamer and Dinegar, 1950), instantaneous nucleation is

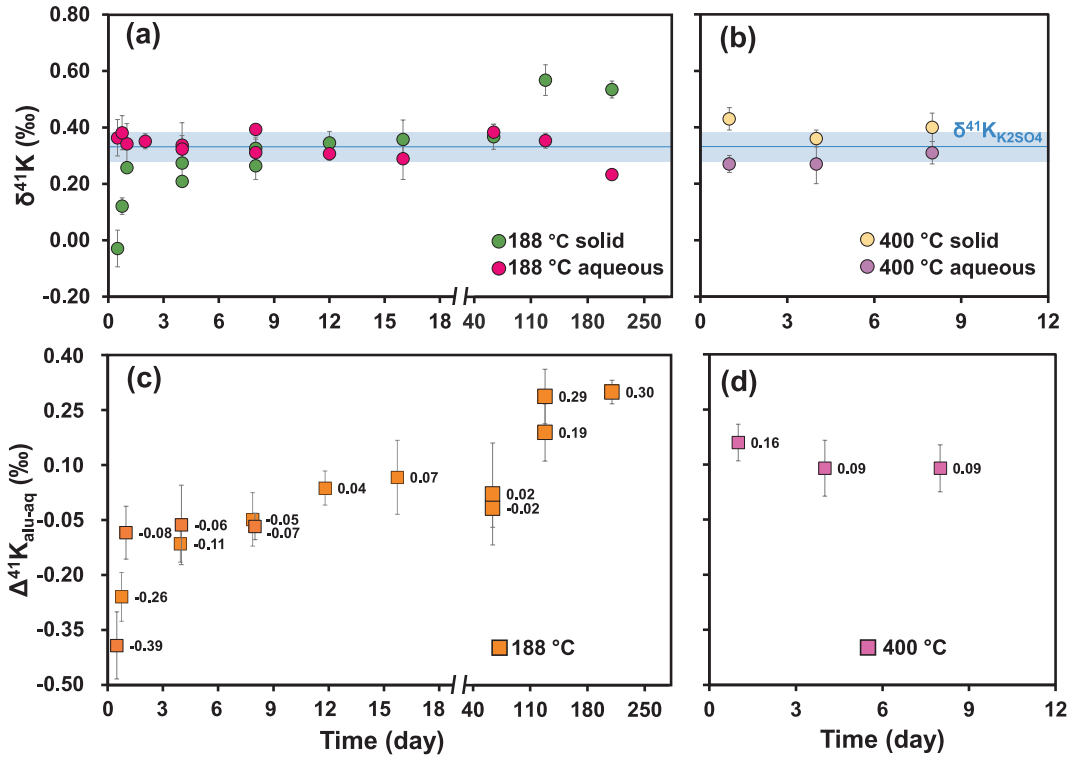

Fig. 5. Potassium (K) isotope data for the time series experiments. (a, c) The $\delta^{41}K$ and $\Delta^{41}K_{alu\text{-}aq}$ values for alunite synthesized with different reaction time at 188°C. (b, d) The $\delta^{41}K$ and $\Delta^{41}K_{alu\text{-}aq}$ values for alunite synthesized with different reaction time at 400°C. The shaded area represents the K isotope composition of the initial K_2SO_4 solution.

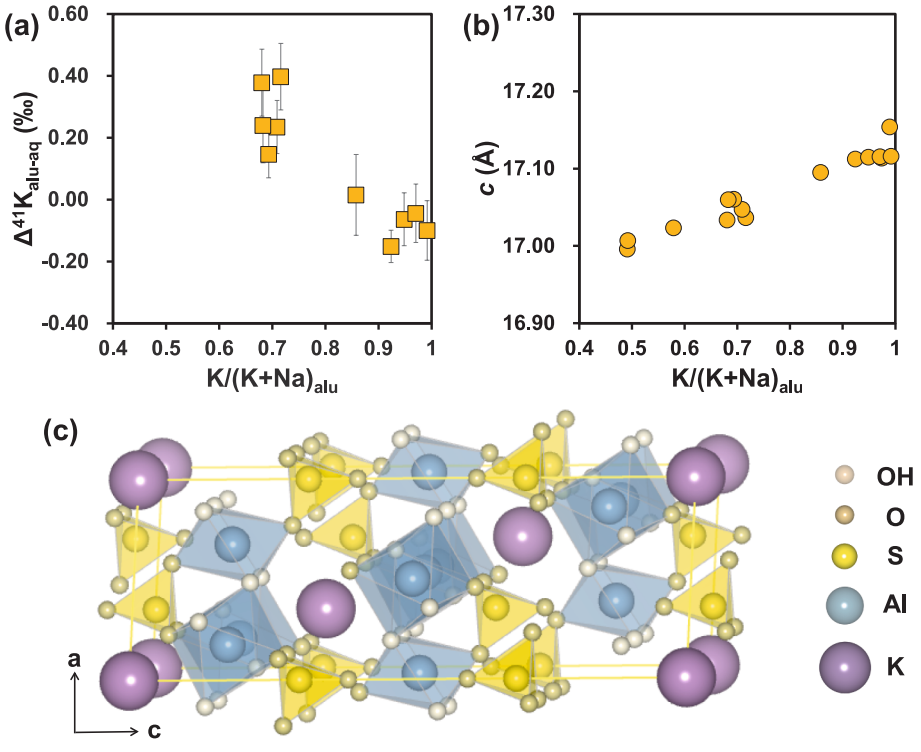

Fig. 6. Relationships between (a) the $\Delta^{41}K_{alu\text{-}aq}$ values and (b) the unit-cell parameter *c* relative to the K/(K + Na) ratio in solid phases at 188°C. (c) Alunite crystal structure. Alunite is a trigonal sulfate mineral with Z = 3, belonging to the space group $R\bar{3}$ m (Wang et al., 1965). The K^+ ions occupy interlayer positions of SO_4^{2-}, Al^{3+}, and OH^-.

followed by diffusion–limited growth. The nucleation process occurs rapidly for homogeneous precipitation when the aqueous solutions are

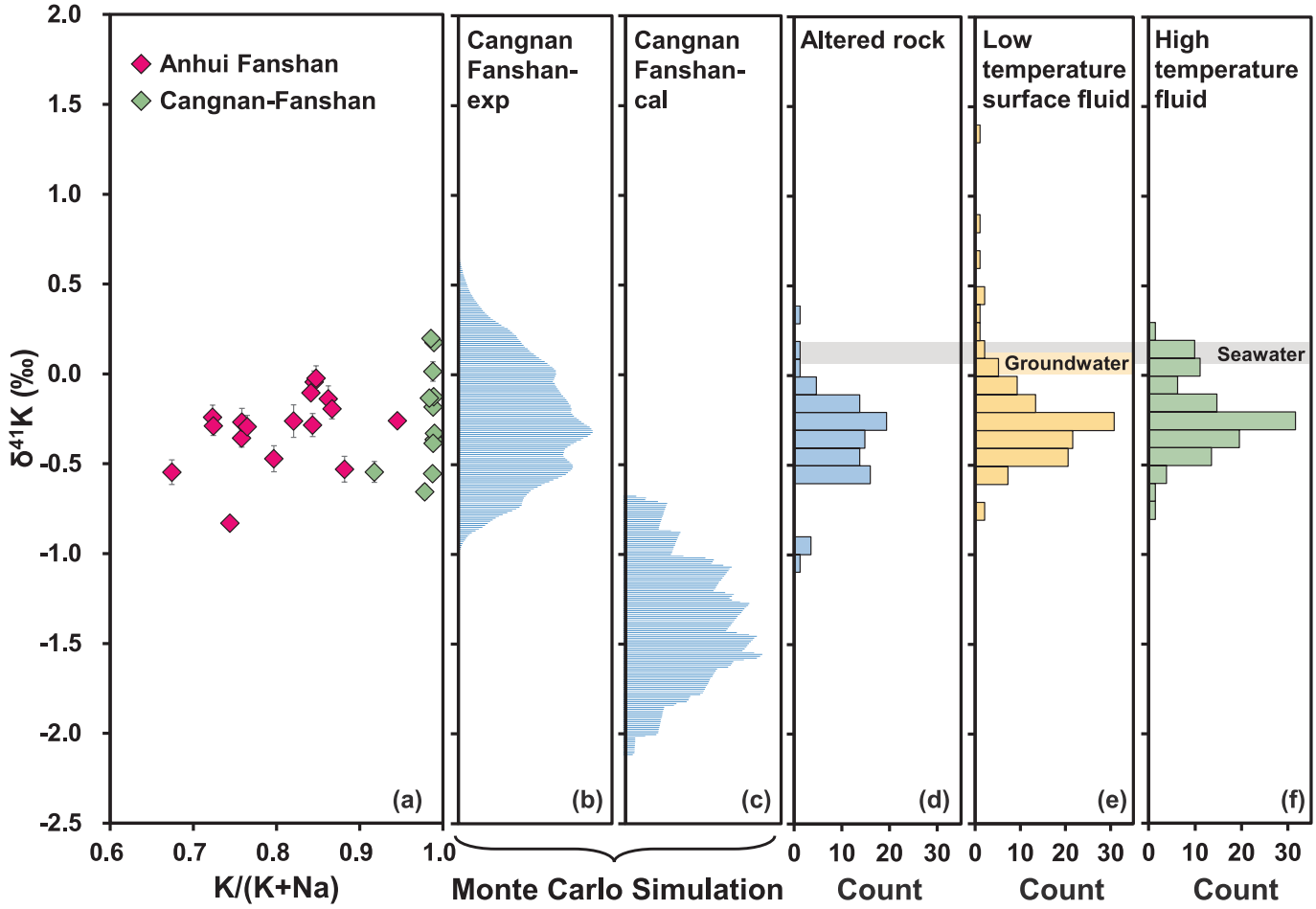

Fig. 7. (a) Potassium (K) isotope compositions of alunite samples from the Zhejiang Cangnan–Fanshan and Anhui-Fanshan deposits. (b) Modeled distributions of $\delta^{41}K$ values of hydrothermal fluids for Cangnan–Fanshan, based on experimental K isotope fractionation factors. (c) Modeled distributions of $\delta^{41}K$ values of hydrothermal fluids for Cangnan–Fanshan, based on theoretical K isotope fractionation factors. (d) Histogram of published K isotope data for hydrothermally altered rocks (Li et al., 2020; Qiu et al., 2024). (e) Histogram of published K isotope compositions of low temperature surface fluids, including data of rivers (Li et al., 2019; Li et al., 2022; Teng et al., 2020; Wang et al., 2021) and salt lakes (He et al., 2025). (f) Histogram of published K isotope compositions of high temperature hydrothermal fluids (Ramos et al., 2022; Zheng et al., 2022). The average seawater value (0.12 ± 0.07‰) is from Hille et al. (2019) and Wang et al. (2020). The groundwater value (0.09 ± 0.05‰) is from Li et al. (2022).

supersaturated. Given the limited number of initial nuclei, solute flux to each particle is enhanced, allowing rapid crystal growth that depletes dissolved ions in the solution. This concentration decline suppresses further nucleation (self–shutdown mechanism), as the system falls below the critical supersaturation required for new nuclei formation. This could explain the larger grain size of alunite formed under lower pH conditions.

By contrast, under elevated pH conditions, the enhanced supersaturation triggers a burst of nucleation, generating a high number density of nuclei favoring subsequent growth–dominated crystallization (Ishizuka et al., 2016). Thus, our pH series experiments strongly imply that the alunite precipitation from hydrothermal fluids in our experiments is dominated by supersaturation–driven kinetic processes that are far from equilibrium.

4.2. Kinetic versus equilibrium K isotope fractionation during alunite precipitation

In the time series experiments at 188°C, the $\Delta^{41}K_{alu-aq}$ values kept increasing throughout the 210 days of experimental duration (Fig. 5c), indicating continuous K isotope exchange between alunite and aqueous solutions. This demonstrates that K isotopes in the solids and aqueous solution did not reach isotopic equilibrium within the experimental timescale. Indeed, theoretical calculations using *ab initio* methods by Li et al. (2019b) suggested much higher equilibrium $\Delta^{41}K_{alu-aq}$ values, which is estimated to be + 1.52‰ at 188°C. The increasing trend of measured $\Delta^{41}K_{alu-aq}$ values in the time series experiments at 188°C suggests the system was initially out of equilibrium but kept evolving towards equilibrium, supporting the high $\Delta^{41}K_{alu-aq}$ value calculated by Li et al. (2019b). Additionally, in the pH series experiments, the measured $\Delta^{41}K_{alu-aq}$ values were also variable and pH dependent, ranging from 0.02‰ at pH = 1.10 to 0.31‰ at pH = 1.66. This can also be explained by the higher equilibrium $\Delta^{41}K_{alu-aq}$ value, because the alunite grains synthesized under higher pH conditions are smaller (Fig. 2), yielding higher specific surface areas and thus faster isotope exchange rates with the surrounding aqueous solutions at equal reaction time. This means that the finer alunite grains in higher pH experiments yielded higher $\Delta^{41}K_{alu-aq}$ values that are closer to equilibrium values. Therefore, both time–series and pH series experiments indicate that the measured $\Delta^{41}K_{alu-aq}$ values in our experiments do not represent equilibrium K isotope fractionation factors between alunite and aqueous K. Instead, the equilibrium $\Delta^{41}K_{alu-aq}$ must be higher than the experimentally measured values. It should be noted that under our experimental conditions, free K^+(aq) is the predominant species (Smith & Martell, 1976; Wagman, 1982). Speciation calculations indicate that, free K^+(aq) comprised of 75–99% of total dissolved K in the aqueous

solutions (Supplementary Material, Text S1), and based on the experimental study of Li et al. (2017), the isotopic effect of sulfate-bonding on K^+ was likely < 0.03‰ under our experimental conditions (Supplementary Material, Text S1).

Additional alunite synthesis experiments were performed at 98°C, 150°C, and 400°C. Measured $\Delta^{41}K_{alu-aq}$ values were consistently lower than those of the theoretical predictions by Li et al. (2019b) (Fig. 8). For reference, Li et al. (2019b) calculated equilibrium $\Delta^{41}K_{alu-aq}$ values of 0.72‰, 1.52‰, 1.80‰, and 2.33‰ at 400°C, 188°C, 150°C, and 98°C, respectively (Fig. 8). The calculated values are one order of magnitude larger than our experimental results. Given the dominance of kinetic K isotope fractionation at 188°C across the experimental timescale (0.75–210 days), this mechanism should persist at lower temperatures (150°C and 98°C). Since the prolonged reactions at 188°C failed to achieve isotopic equilibrium, experiments under lower temperatures would exhibit lower isotope exchange rates (Cole and Chakraborty, 2001), such that the time required to reach equilibrium would far exceed our experimental durations.

At 400°C and 1000 bar, the exchange rate between alunite and fluid is expected to be faster than those at lower temperatures. However, the experimentally measured $\Delta^{41}K_{alu-aq}$ values at 400°C did not show increasing trend with time, in contrast to the time–series experiments at 188°C (Fig. 5). It should be noted that the solid products from the experiments at 400°C consist of a mixture of a small number of large (>100 μm) euhedral alunite crystals with abundant fine (~10 μm) spherical anhedral grains, regardless of reaction time (Fig. S1). The fine grains most likely formed by rapid, supersaturation–driven precipitation during quenching. As a result, the measured $\Delta^{41}K_{alu-aq}$ values at 400°C was still strongly influenced by kinetic isotopic effect. Unfortunately, due to the lack of suitable thermodynamic data for alunite solubility, it is not possible to quantify the contribution of quenching on the alunite precipitates, nonetheless, the experimental results still highlight the dominance of kinetic effects during alunite precipitation.

It is noteworthy that the Na–K series experiments yielded remarkable correlations among $\Delta^{41}K_{alu-aq}$ values, K/(K + Na), and the unit–cell parameter *c* (Fig. 6). Alunite with lower K/(K + Na) ratio has lower unit–cell parameter *c*, which is due to the smaller ion radius of Na^+ than K^+. Accordingly, the average bond length at the G site (the monovalent cation site) of alunite decreases with K/(K + Na) ratios. According to the general theory of isotope fractionation, heavy isotopes favor shorter, stronger bonds (Schauble et al., 2004), consistent with our observation that alunite with lower K/(K + Na) ratio and smaller *c* value displays higher $\Delta^{41}K_{alu-aq}$ values (Fig. 6b). To date, no theoretical studies has explicitly evaluated the on effect of Na substitution for K on K isotope fractionation in alunite. However, *ab initio* calculations show that K–poor alkali feldspar enriches heavy K isotopes compared with K–feldspar or microcline (Li et al., 2019a). It is important to note that the correlation between $\Delta^{41}K_{alu-aq}$ and bond length parameters (*c* value) does not necessarily mean attainment of isotopic equilibrium during the synthesis experiments, because the time–series experiments strongly show that alunite formed after 1 day (the duration of the Na–K series experiments) must be out of isotopic equilibrium with aqueous solution. The systematic increase in $\Delta^{41}K_{alu-aq}$ with increasing K/(K + Na) ratios or *c* values therefore suggests that our experimental data reflect mixed equilibrium and kinetic isotope signals.

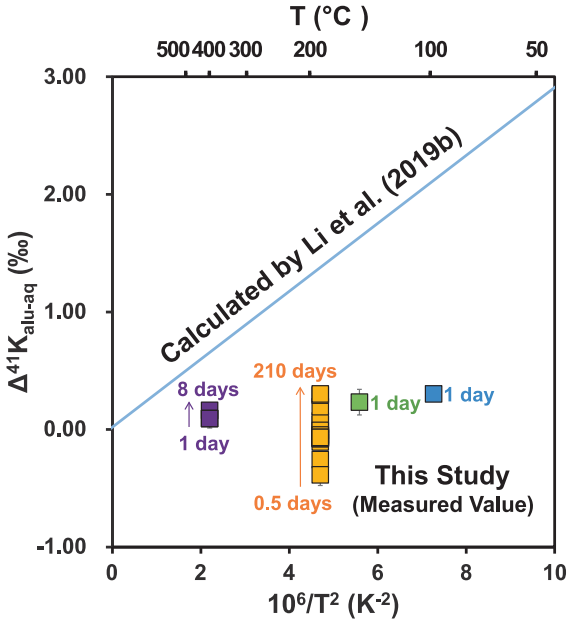

Fig. 8. Comparison of K isotope fractionation factors for alunite between experiments and theoretical predictions. Square symbols represent experimental K isotope data; data points arranged from left to right corresponding to 400°C, 188°C, 150°C, and 98°C.

4.3. Kinetics of surface reaction and isotope exchange during alunite precipitation process

To evaluate the contributions of kinetic and equilibrium isotope fractionations during alunite precipitation, a surface reaction kinetic model developed by DePaolo (2011) is used to interpret the measured apparent K isotope fractionation factors ($\Delta^{41}K_{alu-aq}$). According to the surface reaction kinetic model by DePaolo (2011), bulk isotope fractionation associated with mineral precipitation is controlled by two competing microscopic processes at mineral surface, which can be formulated as:

$$\alpha_p = \left(\frac{r_{solid}}{r_{fluid}}\right) = \frac{\alpha_f}{1 + \frac{R_p}{R_p + R_b}\left(\frac{\alpha_f}{\alpha_{eq}} - 1\right)} \quad (5)$$

where α_p is the effective isotopic fractionation factor for precipitation, which is essentially the experimentally measured $\Delta^{41}K_{alu-aq}$ (i.e., $\Delta^{41}K_{alu-aq} = 1000\ln\alpha_p$), *r* is shorthand for the isotopic ratio of $^{41}K/^{39}K$, α_f is the kinetic isotopic fractionation factors associated with precipitation (forward reaction), and α_{eq} is the equilibrium isotopic fractionation factor. Equation (5) therefore allows a quantitative understanding of the measured K isotope fractionation during alunite precipitation.

Alunite precipitation rates (R_p) can be estimated using the following parameters: time (experiment duration), mass of solid product (calculated from the initial and final solution concentrations), and mineral surface area (estimated from the SEM images), as R_p = solution K consumption/(Surface area × Time). Based on the mass of alunite solid product shown in Fig. 1h, the time required for substantial alunite formation was set to 4 h. Surface area estimates were derived from SEM images processed using PCAS.

There are two existing formulas to estimate the alunite dissolution rates (R_b). According to Miller et al. (2016), alunite dissolution rates are mainly controlled by solution pH, described by the following rate function:

$$\log R_b = -0.133(\pm 0.02)\text{pH} - 10.65(\pm 0.07) \quad (6)$$

Alternatively, according to Acero et al. (2015), alunite dissolution rates are controlled by both temperature and solution pH, following the rate function of:

$$R_b = 10^{-4.4\pm0.5} + \alpha_{H^+}^{0.10\pm0.02} + e^{-32\pm3/RT} \quad (7)$$

Under our experimental conditions, these two rate functions yield different R_b values: 1.76 × 10^{-11} to 1.92 × 10^{-11} mol•m^{-2}•s^{-1} using equation 6 and 7.86 × 10^{-9} to 8.40 × 10^{-9} mol•m^{-2}•s^{-1} using equation (7), based on the pH data in Table S1. The two rates differ by over 400 times at 188°C. It is important to note that these empirical correlations

likely arise because pH (and temperature) are key variables affecting the saturation state (Ω) of the solution with respect to alunite. The fundamental driver for dissolution is the degree of undersaturation (1–Ω), which depends on the activities of all constituent ions (K^+, Al^{3+}, SO_4^{2-}, OH^-/H^+). In this study, our calculations are based on the consistent initial conditions maintained across the experimental series and the fact that K^+ and SO_4^{2-} were always in excess; consequently, the variation in Ω should be predominantly driven by pH. Nonetheless, the calculated R_b are still several orders of magnitude lower than the precipitation rates (Fig. 9). As shown in Fig. 9, according to surface reaction kinetic model, the high R_p/R_b dictates that K isotope fractionation during alunite precipitation remains in the kinetic–dominated realm, regardless the values of the equilibrium or kinetic isotope fractionation factors (α_f, α_{eq}).

The measured $\Delta^{41}K_{alu-aq}$ (–0.39 to 0.30‰) are 1.91–1.22‰ lower than the theoretically calculated equilibrium K isotope fractionation factors at 188°C, suggesting the kinetic isotope effects cause remarkable relative enrichment of light K isotopes in alunite during its precipitation. For comparison, the kinetic isotope fractionation factor for K ion desolvation is –2.4 ± 0.4‰ (Hofmann et al., 2012), the kinetic isotope fractionation factor for K ion diffusion in aqueous solution is –1.4 to –2.1‰ (Bourg et al., 2010; Li et al., 2024). These two factors are comparable with the offsets between measured and theoretically predicted $\Delta^{41}K_{alu-aq}$ values, implying that at least one of the mechanisms had exerted kinetic isotope effect upon alunite precipitation. However, it is unlikely that both mechanisms superimposed their full kinetic isotopic effects during alunite precipitation, otherwise the measured $\Delta^{41}K_{alu-aq}$ value would be as low as –2.31 to –2.98‰ (Fig. 9), which is not supported by observation.

Additionally, it is possible to use the time–series experiment isotope data to constrain the K exchange rate between alunite and aqueous solutions. The initially precipitation of alunite yielded $\Delta^{41}K_{alu-aq}$ value of –0.39‰, which increased to 0.30‰ after 210 days due to continuous mineral–fluid isotope exchange. If we assume the exchanged proportion of alunite had reached isotopic equilibrium with the aqueous solution, then the degree of isotope exchange can be quantified as $(\Delta^{41}K_{day0}-\Delta^{41}K_{day210})/(\Delta^{41}K_{day0}-\Delta^{41}K_{eq})$ (Li et al., 2014), which is 36% after 210 days. This value, combined with the average surface area of alunite crystals, yields an exchange rate of 4.02×10^{-10} mol•m^{-2}•s^{-1}. We note that the calculated degree of K isotope exchange and exchange rate are dependent on $\Delta^{41}K_{eq}$, which is based on theoretical calculation of Li et al. (2019b) that has not been experimentally verified. Such calculated exchange rate could be different if the real $\Delta^{41}K_{eq}$ differs from the theoretical calculation of Li et al. (2019b). Nonetheless, our time-series experiments have confirmed the direction of $\Delta^{41}K_{eq}$ by Li et al. (2019b) are correct. Further, our calculated exchange rate is between the alunite dissolution rates (R_b) calculated based on the equations of Miller et al. (2016) and Acero et al. (2015), corroborating the validity of the estimation based on K isotope fractionation factors.

The non–equilibrium K isotope fractionation during alunite precipitation is in distinct contrast to the cases of K–bearing simple salts (e.g., KCl, K_2SO_4) and double salts (e.g., carnallite), which can achieve K isotopic equilibrium with the surrounding brines quickly under laboratory time scale and also in natural settings (Li et al., 2017; Xia et al., 2024). Such contrast correlates with the huge difference in mineral solubility, that K–bearing simple salts and double salts studied by Li et al. (2017) and Xia et al. (2024) are all highly soluble, with solubilities reaching several moles per liter in aqueous solution. As soluble minerals also have high dissolution rates (R_b), the high R_b rates of K–bearing simple salts and double salts ensures fast isotope exchange between the salts and fluids, facilitating equilibration for K isotopes, which is not the case for alunite.

4.4. Implications for relevant geological and planetary studies

The stark contrast between experimentally measured and theoretically calculated K isotope fractionation factors for alunite raises a critical question of how K isotope data of natural alunite samples should be interpreted. By answering this question, insights could be gained regarding whether the natural alunite precipitation processes are kinetically dominated. The best approach may be the measurements of paired fluid and mineral samples from an active alunite–forming hydrothermal system. However, such samples are unavailable for this study. Therefore, we turned to fossil high–sulfidation hydrothermal systems, the alunite–rich ore deposits, and analyzed various natural alunite samples, followed by attempts to derive and evaluate the K isotope composition of hydrothermal fluids.

Natural alunite samples from the two studied deposits show differences in geological background and mineral occurrences (He et al.,

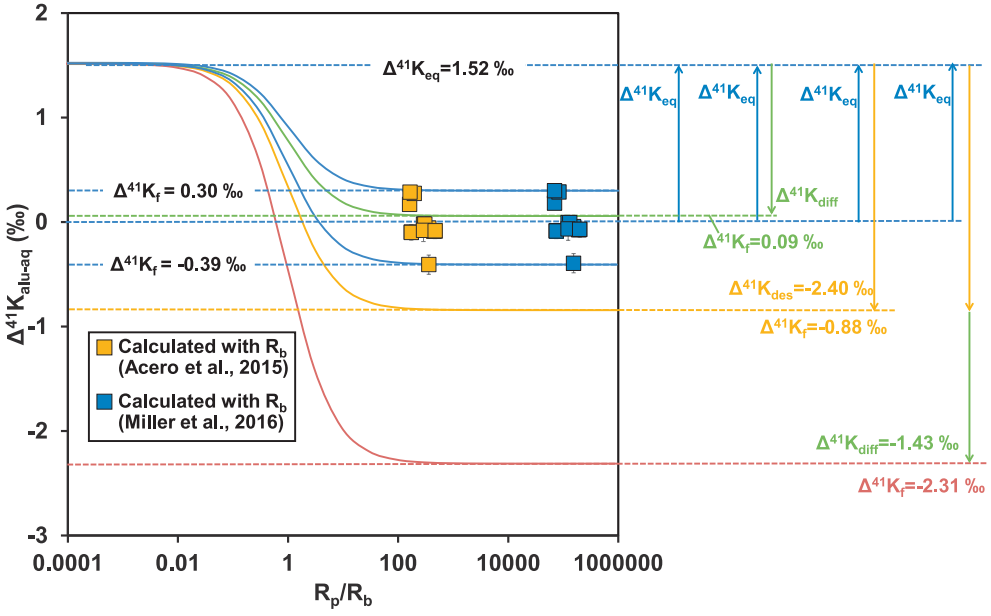

Fig. 9. Apparent K isotope fractionation factor during alunite precipitation as a function of R_p/R_b. Squares represent experimental data from this study. The R_b was calculated based on Miller et al. (2016) and Acero et al. (2015). $\Delta^{41}K_{eq}$, $\Delta^{41}K_{diff}$, $\Delta^{41}K_{des}$ refers to equilibrium K isotope fractionation, diffusion-driven K isotope fractionation, and kinetic isotope effect associated with desolvation of K^+ ion, respectively.

2009; Li et al., 2020a, 2020b; Lv, 2002; Tang, 2008), and additionally, in mineral chemistry. Alunite samples from the Cangnan–Fanshan deposit are in general more K–rich, with K/(K + Na) ratios mostly above 0.95, whereas the alunite samples from the Anhui–Fanshan deposit contain significantly higher Na, with K/(K + Na) ratios mostly varying between 0.7 and 0.85 (Fig. 7a). Such K/(K + Na) ranges are covered by our experimental settings (i.e., the Na/K series experiment), so are the forming temperature ranges (i.e., 98–400°C in experiment, 260–290°C in Anhui–Fanshan deposit, and 175–300°C in Cangnan–Fanshan deposit). Therefore, it is possible to estimate the K isotope compositions of the hydrothermal fluids from which alunite precipitated based on the experimentally measured $\Delta^{41}K_{alu-aq}$ factors in this study. A Monte Carlo approach was applied to account for the unspecified temperature for each alunite sample and to bridge the gaps between the discrete experimentally derived $\Delta^{41}K_{alu-aq}$ factors. This modeling is similar to the approach reported by Wang et al. (2021) and the details are provided in Supplementary Material, Text S2. The Monte Carlo modeling yielded broadly overlapping distribution patterns of K isotope compositions for the hydrothermal fluids in the two deposits, which have $\delta^{41}K$ values clustering around 0.5‰ to –0.8‰ (Fig. 7b).

We also performed Monte Carlo modeling under the alternative assumption that the alunite samples were in isotopic equilibrium with hydrothermal fluids during alunite precipitation. In this case, the temperature dependent K isotope fractionation function proposed by Li et al. (2019b) is applied to the Cangnan–Fanshan alunite samples because the effect of Na on equilibrium K isotope fractionation factor has not been quantified by *ab initio* calculation studies. The modeling results are also presented in Fig. 7c, which shows that the $\delta^{41}K$ values of aqueous K^+ in equilibrium with alunite would be much lower, clustering at –1‰ to –2‰. This range is remarkably lower than the $\delta^{41}K$ values estimated based on experimental results.

Although direct measurements of hydrothermal fluid K isotopes remain unavailable, insights can be gained through comparison with published K isotope data of various geofluids and rocks altered by hydrothermal fluids (Fig. 7d–f). The $\delta^{41}K$ values of river waters and groundwaters cluster between –0.6‰ and 0.1‰. This range is similar to those of hydrothermal fluids from mid–ocean, which is well above the modelled $\delta^{41}K$ range for hydrothermal fluids at Cangnan–Fanshan assuming equilibrium between alunite and aqueous K^+. This either rules out the significant contribution of river and groundwater to K in the alunite in the Cangnan–Fanshan system, or invalidates the equilibrium K isotope fractionation for natural alunite precipitation if hydrothermal fluids had $\delta^{41}K$ values similar to surface waters.

Hydrothermally altered rocks in porphyry Cu deposits and orogenic gold deposits also display a $\delta^{41}K$ range that overlaps with those of alunite and rivers, mostly between –0.6‰ and 0.1‰ (Fig. 7d). The dominant K–bearing phases in these altered rocks include K–feldspar and sericite (Li et al., 2020; Qiu et al., 2024). According to theoretical calculations, the K isotope fractionation factors between K–feldspar, sericite and aqueous solutions are small ($\Delta^{41}K_{feldspar-fluid} \approx 0.016$‰, Zeng et al. 2019), the $\delta^{41}K$ of the hydrothermal fluids are expected to be similar to those of altered rocks. This is supported by hydrothermal fluids from mid–ocean ridge (MOR) hydrothermal systems that have $\delta^{41}K$ values broadly similar to MOR basalts (i.e., ~–0.4‰, Ramos et al. 2022; Zheng et al. 2022). K isotope fractionation factors associated with hydrothermal alteration were calculated to be small, no greater than 0.6‰ (Li et al., 2020; Qiu et al., 2024). Taken together, the various geofluids studied so far generally have $\delta^{41}K$ values in the range of –0.6 to 0.1‰, which are consistent with the inferred K isotope composition of hydrothermal fluids responsible for alunite precipitation in the Cangnan–Fanshan deposit, based on the experimentally calibrated $\Delta^{41}K_{alu-aq}$ factors calibrated in this study (Fig. 7b). It is highly unlikely, if not impossible, that the hydrothermal fluids of Cangnan–Fanshan deposit had low $\delta^{41}K$ range of –2 to –1‰, as calculated based on equilibrium isotope fractionation factors (Fig. 7c).

Therefore, non–equilibrium K isotope fractionations occur during alunite precipitation not only in our laboratory synthesis experiments, but also in different natural hydrothermal systems. In both cases, kinetic isotope effects dominated during alunite precipitation, and such kinetic effects were not erased by subsequent isotope exchange between alunite and aqueous fluids, although the time–series experiment in this study showed that the exchange continued throughout the 210 days of experiments. By a simple comparison of the experimental $\Delta^{41}K_{alu-aq}$ and theoretically predicted equilibrium values, an isotope exchange degree of 36% was estimated towards isotopic equilibrium (see discussion in section 4.3). It should be noted that the isotope exchange between alunite and aqueous solution does not necessarily proceed in linear fashion. Stoffregen et al. (1994b) suggested that the cation exchange of alunite could follow first–order rate law or pseudo–second–order rate law. Using a first–order kinetic model (for details see Supplementary Material, Text S3), it is estimated that 3,411–5,117 days (9–14 years) are needed to reach > 99% isotope exchange towards isotope equilibrium. Using a pseudo–second–order model, the time required to reach the same degree of isotope equilibrium increases to 65,433–660,278 days (179–1809 years) (Fig. 10).

Combining our experimental data and previous studies, we estimated that 10–1000 years may be required for K isotope equilibration between alunite and aqueous fluids under hydrothermal conditions. Again, we note that these time estimates stem from a number of assumptions including the degree of isotope exchange that are ultimately dependent on the true equilibrium K isotope fractionation factor for alunite, for which we relied on the calculation study of Li et al. (2019b) that is yet to be verified. Nonetheless, such time span (10–1000 years) is well above the duration of laboratory experiments, but is short geologically speaking. The apparent lack of attainment of K isotope equilibrium for alunite in Cangnan–Fanshan system, therefore, suggests that the alunite was formed in rapid events, when the fluid activities were transient and could not be stable to exchange with alunite crystals for thousands of years. Therefore, the high–sulfidation hydrothermal systems where alunite form should be highly dynamic in their hydrology. This inference is further supported by observations from other alunite–bearing hydrothermal systems. In the Potrerillos district, Chile, hypogene alunite exhibits tabular habits with grain sizes > 200 μm, whereas steam–heated

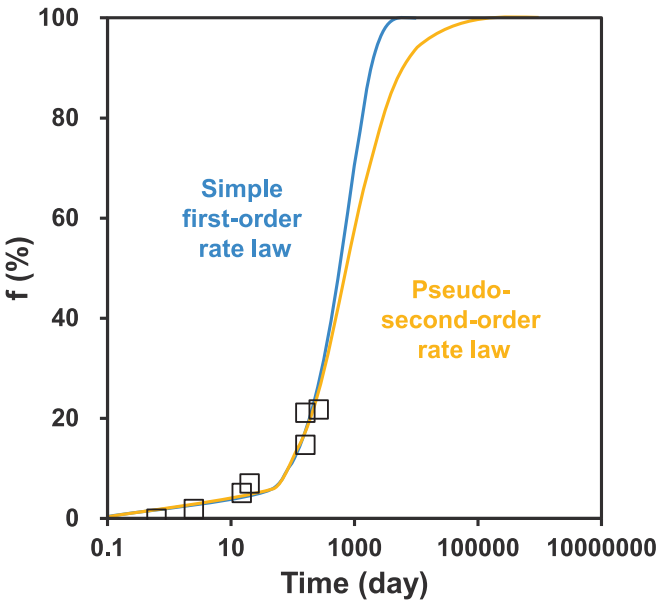

Fig. 10. Comparison of first-order and pseudo-second-order kinetic models for K isotope exchange in alunite. The open squares represent the experimental data points calculated from the time-series experiments. The solid lines represent the best fits to the data using two different kinetic models. The upper blue curve depicts a first-order rate law, while the lower brown curve depicts a pseudo-second-order rate law.

alunite is characterized by smaller crystals (<100 μm), reflecting differences in precipitation rates (Morales-Leal et al., 2023). In the Kuh–e–Lakht epithermal system, Iran, alunite crystals display well–developed oscillatory zoning with alternating K–rich and Na–rich bands, which is a hallmark of rapid, non–equilibrium growth under fluctuating fluid conditions (Naderi et al., 2024). The preservation of such delicate oscillatory zoning, without diffusive homogenization, attests to rapid precipitation and subsequent isolation from the fluid. Collectively, these occurrences provide evidence that alunite precipitation in diverse hydrothermal settings is dominated by rapid, kinetically controlled processes.

We note that the alunite or alunite–group minerals on Mars may be treated differently than alunite from hydrothermal deposits on Earth. Orbital and *in situ* observations have revealed a spectrum of possible formation environments on Mars. In evaporative environments such as concentrated sulfate brines in ponds or basins (Bristow et al., 2018), prolonged fluid contact times could potentially permit isotopic equilibrium. In volcanic–hydrothermal systems analogous to those documented at Cross crater, Terra Sirenum, where alunite occurs as massive, fracture–controlled advanced argillic alteration assemblages associated with regional magmatism and extensional faulting (Ehlmann et al., 2016). In impact–generated hydrothermal systems, although alunite has not yet been unequivocally detected in such contexts on Mars, terrestrial analogs (e.g., Ries crater, Chicxulub) and nakhlite meteorite alteration assemblages demonstrate that impact melt sheets can sustain low–temperature, acid–sulfate hydrothermal activity capable of precipitating alunite–group minerals (Martin et al., 2017; Schwenzer et al., 2012). Even more ephemeral processes, such as recurring slope lineae or localized spring discharges, may also host transient acid–sulfate alteration, though the mineralogical expression and preservation potential of such short–lived systems remain poorly constrained. Our experiments show that kinetic fractionation dominates under rapid precipitation regimes typical of volcanic–hydrothermal systems, and that isotopic equilibration may require 10^3 to 10^4 years under hydrothermal conditions (Fig. 10), providing a framework for interpreting future K isotope measurements of Martian alunite. Through combined analysis of alunite K isotope composition, crystal morphology, solid–solution chemistry, and paragenetic context, it may be more feasible to distinguish the aqueous alteration history and paleoenvironmental conditions recorded by Martian alunite.

Moreover, it is worthy to note that in contrast to the distinct correlation observed between $\Delta^{41}K_{alu-aq}$ and K/(K + Na) in experimental samples (Fig. 6a), no significant correlation is found between $\delta^{41}K$ and K/(K + Na) in natural alunite (Fig. 7a). This discrepancy may be attributed to the continuous evolution of ore–forming fluids. We assume that early alunite precipitation preferentially depletes K (relative to Na) from the fluid, thereby lowering the K/(K + Na) ratio of the residual fluid. Given that $\Delta^{41}K_{alu-aq} > 0$, later–stage fluids would possess lower K/(K + Na) ratios and lower $\delta^{41}K$ values. Meanwhile, experiments demonstrate that lower K/(K + Na) ratios generally correspond to larger $\Delta^{41}K_{alu-aq}$ values. Consequently, the opposing effects of fluid lightening and enhanced fractionation may compensate each other, obscuring obvious correlation between $\delta^{41}K$ and K/(K + Na) in natural samples. This further supports the dominance of kinetic fractionation during natural alunite precipitation and implies that the $\delta^{41}K$ of ore–forming fluids is generally lower than that of associated alunite.

5. Conclusions

This study demonstrates that K isotope fractionation during alunite precipitation under hydrothermal conditions is dominated by kinetic effects rather than equilibrium processes. In time series experiments conducted at 188°C, the apparent K isotope fractionation ($\Delta^{41}K_{alu-aq}$) evolved continuously from –0.39‰ to 0.30‰ over 210 days, with no isotopic equilibrium achieved even after prolonged reaction times. Measured $\Delta^{41}K_{alu-aq}$ values across various conditions are consistently and significantly lower than theoretical equilibrium predictions. This discrepancy, coupled with observed correlations between fractionation, crystal morphology, and mineral chemical composition (e.g., K/Na ratio), corroborating the dominance of kinetic processes in K isotope partitioning during alunite crystallization.

By comparing with reported K isotope data of geofluids, we found that the $\delta^{41}K$ variations of natural alunite samples closely match the experimentally derived kinetic fractionation, rather than following equilibrium fractionation models. This indicates that the formation of natural alunite is similarly controlled by kinetics. By extrapolating laboratory time–series data, we estimated that the time required for potassium isotope fractionation between alunite and fluids to reach equilibrium may be 10–1000 years, which is a short geological time span. Therefore, we propose that alunite formed during rapid events, when fluid activities were transient and unable to remain stable enough to exchange with alunite crystals over thousands of years. These findings underscore the necessity of applying experimentally determined kinetic isotope fractionation to interpret K isotope signatures in natural alunite, thereby enhancing their utility in tracing fluid–rock processes on Earth and Mars.

Data availability

The data of experimental and natural alunite samples in this work are available through Mendeley Data at: https://doi.org/10.17632/22tj65rjkk.1.

CRediT authorship contribution statement

Yuqi Li: Writing – original draft, Visualization, Investigation. **Yang Zhang:** Validation, Investigation. **Xudong Che:** Supervision, Resources. **Zhimin Tang:** Methodology, Investigation. **Weiqiang Li:** Writing – review & editing, Writing – original draft, Supervision, Resources, Project administration, Funding acquisition, Formal analysis, Conceptualization.

Declaration of competing interest

The authors declare that they have no known competing financial interests or personal relationships that could have appeared to influence the work reported in this paper.

Acknowledgements

This research was financially supported by the National Natural Science Foundation of China (No. 42425301 to WL). We are grateful to Feipeng Fan from the Nanjing Center of China Geological Survey for providing the field samples of the Cangnan–Fanshan alunite deposit. We also thank Shichao An for his assistance in potassium isotope ratio measurements, as well as Jun Mu and Haoran Xu for their support during field sampling in the Anhui–Fanshan alunite deposit.

Appendix A. Supplementary material

Supplementary material to this article can be found online at https://doi.org/10.1016/j.gca.2026.03.040. Details on the SEM–EDS results of 400°C experiments, map of the study area of Anhui–Fanshan and Cangnan–Fanshan are included in Supplementary Material. The isotopic and mineralogical parameters of the alunite samples are provided in Supplementary Table S1–S4. The Monte Carlo simulation process, the geochemical modeling with GWB, the procedure employed to fit the experimental alkali exchange data to the first–order and pseudo–second–order rate laws are provided in Supplementary Text S1-S3.

References

Acero, P., Hudson-Edwards, K.A., Gale, J.D., 2015. Influence of pH and temperature on alunite dissolution: rates, products and insights on mechanisms from atomistic simulation. Chem. Geol. 419, 1–9.

An, S., Luo, X., Li, W., 2022. Precise measurement of 41K/39K ratios by high–resolution multicollector inductively coupled plasma mass spectrometry under a dry and hot plasma setting. Rapid Commun. Mass Spectrom. 36 (11), e9289.

Bayliss, P., Kolitsch, U., Nickel, E.H., Pring, A., 2010. Alunite supergroup: recommended nomenclature. Mineral. Mag. 74 (5), 919–927.

Bissig, T., Riquelme, R., 2010. Andean uplift and climate evolution in the southern Atacama Desert deduced from geomorphology and supergene alunite–group minerals. Earth Planet. Sci. Lett. 299 (3–4), 447–457.

Bourg, I., Richter, F., Christensen, J., Sposito, G., 2010. Isotopic mass dependence of metal cation diffusion coefficients in liquid water. Geochim. Cosmochim. Acta 74 (8), 2249–2256.

Bristow, T., Rampe, E., Achilles, C., Blake, D., Chipera, S., Craig, P., Crisp, J., Des Marais, D., Downs, R., Gellert, R., Grotzinger, J., Gupta, S., Hazen, R., Horgan, B., Hogancamp, J., Mangold, N., Mahaffy, P., McAdam, A., Ming, D., Morookian, J., Morris, R., Morrison, S., Treimans, A., Vanimanm, D., Vasavada, A., Yen, A., 2018. Clay mineral diversity and abundance in sedimentary rocks of Gale crater. Mars. Sci. Adv. 4 (6), eaar3330.

Cole, D.R., Chakraborty, S., 2001. Rates and Mechanisms of Isotopic Exchange. Rev. Mineral. Geochem. 43 (1), 83–223.

Coward, A.J., Slim, A.C., Brugger, J., Wilson, S., Williams, T., Pillans, B., Maksimenko, A., 2023. Mineralogy and geochemistry of pattern formation in zebra rock from the East Kimberley. Australia. Chem. Geol. 622, 121336.

DePaolo, D.J., 2011. Surface kinetic model for isotopic and trace element fractionation during precipitation of calcite from aqueous solutions. Geochim. Cosmochim. Acta 75 (4), 1039–1056.

Duan, G., Wu, C., Baker, M.J., Qi, J., Xu, C., Zhang, L., 2022. Evolution and genesis of hydrothermal fluids for the cretaceous Dongnan Cu deposit, Zijinshan ore district (SE China). Ore Geol. Rev. 144, 104844.

Ehlmann, B.L., Swayze, G.A., Milliken, R.E., Mustard, J.F., Clarks, R.N., Murchie, S.L., Breit, G.N., Wray, J.J., Gondet, B., Poulet, F., Carter, J., Calvin, W.M., Benzel, W.M., Seelos, K.D., 2016. Discovery of alunite in Cross crater, Terra Sirenum, Mars: evidence for acidic, sulfurous waters. Am. Mineral. 101 (7–8), 1527–1542.

Fan, Y., Zhou, T., Yuan, F., Tang, M., Zhang, L., Ma, L., Xie, J., 2010. High sulfidation epithermal hydrothermal system in Lu–Zong volcanic basin: evidence from geological characteristics and sulfur isotope data of Fanshan alunite deposit. Acta Petrol. Sin. 26, 3657–3666.

Fielding, S.J., 1980. Crystal chemistry of the oxonium alunite–potassium alunite series. M.S. thesis, Lehigh University, Bethlehem, PA, USA.

He, Y., Zhang, Q., Zhu, C., Wang, D., 2009. The significance of stable isotopic characteiustics in the classification of alunite ore deposits. Acta. Mineral. Sin. 29, 95–102.

He, M., Cheng, Y., Chen, J., Li, Z., Deng, L., Ren, T., Luo, J., Rao, H., 2025. Potassium isotope constraints on brine sources and evolution in Qaidam Basin, Tibetan Plateau. Ore Geol. Rev. 181, 106632. https://doi.org/10.1016/j.oregeorev.2025.106632.

Hedenquist, J.W., Arribas, A., 2022. Exploration Implications of Multiple Formation Environments of Advanced Argillic Minerals. Econ. Geol. 117 (3), 609–643.

Hedenquist, J.W., Watanabe, Y., Arribas, A., 2020. Hypogene alunite from the El Salvador district, Chile, indicates potential for a blind porphyry copper center. Econ. Geol. 115 (2), 231–239.

Hille, M., Hu, Y., Huang, T., Teng, F., 2019. Homogeneous and heavy potassium isotopic composition of global oceans. Sci. Bull. 64 (23), 1740–1742. https://doi.org/10.1016/j.scib.2019.09.024.

Hofmann, A., Bourg, I., DePaolo, D., 2012. Ion desolvation as a mechanism for kinetic isotope fractionation in aqueous systems. PNAS 109 (46), 18689–18694.

Ishizuka, S., Kimura, Y., Yamazaki, T., Hama, T., Watanabe, N., Kouchi, A., 2016. Two–Step Process in Homogeneous Nucleation of Alumina in Supersaturated Vapor. Chem. Mater. 28 (23), 8732–8741.

Li, S., Li, W., Beard, B.L., Raymo, M.E., Wang, X., Chen, Y., Chen, J., 2019. K isotopes as a tracer for continental weathering and geological K cycling. PNAS 116 (18), 8740–8745.

Li, W., Beard, B., Li, C., Johnson, C., 2014. Magnesium isotope fractionation between brucite [Mg(OH)2] and Mg aqueous species: implications for silicate weathering and biogeochemical processes. Earth Planet. Sci. Lett. 394, 82–93.

Li, W., Beard, B.L., Li, S., 2016. Precise measurement of stable potassium isotope ratios using a single focusing collision cell multi–collector ICP–MS. J. Anal. At. Spectrom 31 (4), 1023–1029.

Li, X., Han, G., Liu, M., Liu, J., Zhang, Q., Qu, R., 2022. Potassium and its isotope behaviour during chemical weathering in a tropical catchment affected by evaporite dissolution. Geochim. Cosmochim. Acta 316, 105–121. https://doi.org/10.1016/j.gca.2021.10.009.

Li, W., Ji, Z., Luo, X., Li, Y., 2024. Isotope fractionation of alkaline and alkaline–earth elements (Li, K, Rb, Mg, Ca, Sr, Ba) during diffusion in aqueous solutions. Geochim. Cosmochim. Acta 370, 104–112.

Li, W., Kwon, K.D., Li, S., Beard, B.L., 2017. Potassium isotope fractionation between K–salts and saturated aqueous solutions at room temperature: laboratory experiments and theoretical calculations. Geochim. Cosmochim. Acta 214, 1–13.

Li, Y., Wang, W., Huang, S., Wang, K., Wu, Z., 2019a. First–principles investigation of the concentration effect on equilibrium fractionation of K isotopes in feldspars. Geochim. Cosmochim. Acta 245, 374–384.

Li, Y., Wang, W., Wu, Z., Huang, S., 2019b. First–principles investigation of equilibrium K isotope fractionation among K–bearing minerals. Geochim. Cosmochim. Acta 264, 30–42.

Li, W., Zhao, S., Wang, X., Li, S., Wang, G., Yang, T., Jin, Z., 2020. Fingerprinting hydrothermal fluids in porphyry Cu deposits using K and Mg isotopes. Sci. China-Earth Sci. 63 (1), 108–120.

Li, X., Zhou, T., Liu, Y., Chen, J., Zhang, L., White, N.C., Xie, J., 2019. Geochronology and geological significances of Fanshan lithocap in Luzong Basin, Anhui Province. Acta Petrol. Sinica 35 (12), 3782–3796.

Li, X., Zhou, T., White, N.C., Fan, Y., Chen, J., Liu, Y., 2020a. Genesis of Fanshan lithocap, Luzong volcanic basin, Anhui Province, China – Indications from alunite and pyrite isotopes. Ore Geol. Rev. 127, 103802.

Li, X., Zhou, T., White, N.C., Fan, Y., Zhang, L., Xie, J., Liu, Y., Xiao, X., 2020b. Formation of the Fanshan lithocap and implications for exploration in the Luzong Basin, Anhui Province. China. Ore Geol. Rev. 118, 103314.

Liu, C., Shi, B., Zhou, J., Tang, C., 2011. Quantification and characterization of microporosity by image processing, geometric measurement and statistical methods: application on SEM images of clay materials. Appl. Clay Sci. 54 (1), 97–106.

Lv, H., 2002. Geological characteristics and genesis types of alunite deposits in Zhejiang Province. Geol. Chem. Miner. 03, 146–150.

Manalo, P., Takahashi, R., Imai, A., Parcon–Calamohoy, R.R., de los Santos, M., Subang, L., Alburo, G.C., 2022. Heterogeneity of mineral chemistry and sulfur isotopic composition of alunite in the Mankayan lithocap, northern Luzon, Philippines. Ore Geol. Rev. 146, 104959. DOI: 10.1016/j.oregeorev.2022.104959.

Martin, P.E., Farley, K.A., Baker, M.B., Malespin, C.A., Schwenzer, S.P., Cohen, B.A., Mahaffy, P.R., McAdam, A.C., Ming, D.W., Vasconcelos, P.M., Navarro-González, R., 2017. A Two–Step K–Ar Experiment on Mars: dating the Diagenetic Formation of Jarosite from Amazonian Groundwaters. J. Geophys. Res.–planets 122 (12), 2803–2818.

Mederer, J., Moritz, R., Chiaradia, M., Spikings, R., Spangenberg, J.E., Selby, D., 2019. Ore Formation during Jurassic Subduction of the Tethys along the Eurasian Margin: constraints from the Kapan District, Lesser Caucasus, Southern Armenia. Econ. Geol. 114 (7), 1251–1284.

Miller, J.L., Madden, A.S.E., Phillips-Lander, C.M., Pritchett, B.N., Madden, M.E.E., 2016. Alunite dissolution rates: dissolution mechanisms and implications for Mars. Geochim. Cosmochim. Acta 172, 93–106.

Mills, S.J., Hatert, F., Nickel, E.H., Ferraris, G., 2009. The standardisation of mineral group hierarchies: application to recent nomenclature proposals. Eur. J. Mineral. 21 (5), 1073–1080.

Morales-Leal, J., Campos, E., Kouzmanov, K., Riquelme, R., 2023. Alunite supergroup minerals from advanced argillic alteration assemblage in the southern Atacama Desert as indicators of paleo–hydrothermal and supergene environments. Miner. Deposita 58 (3), 593–615.

Naderi, M., Modabberi, S., Tarantola, A., Haroni, H., 2024. Mineralogical and geochemical constraints on the origin of alunite and APS minerals from advanced argillic alteration systems: a case study from Kuh–e–Lakht Au–Ag–Cu mineralization, NE Isfahan. Iran. J. Geochem. Explor. 262, 107467.

Parker, R.L., 1962. Isomorphous substitution in natural and synthetic alunite. Am. Mineral. 47 (1–2), 127–136.

Perello, J., Brockway, H., Garcia, A., 2020. A minimum Thanetian (Paleocene) age for the African Surface in the Eritrean highlands, Northeast Africa. J. Afr. Earth Sci. 164, 103782.

Qiu, J., Liu, W., Chen, J., Lai, X., Zhong, X., Li, J., Long, H., 2024. Alteration mineralogy, characteristics and shortwave infrared spectroscopy of white mica in the Zijinshan ore field, Fujian Province: implications for porphyry Cu prospecting. Ore Geol. Rev. 168, 106065.

Quang, C.X., Clark, A.H., Lee, J.K.W., Hawkes, N., 2005. Response of supergene processes to episodic Cenozoic uplift, pediment erosion, and ignimbrite eruption in the porphyry copper province of southern Peru. Econ. Geol. 100 (1), 87–114.

Ramos, D., Nielsen, S., Coogan, L., Scheuermann, P., Seyfried, W.J., Higgins, J., 2022. The effect of high–temperature alteration of oceanic crust on the potassium isotopic composition of seawater. Geochim. Cosmochim. Acta 339, 1–11.

Rampe, E.B., Bristow, T.F., Morris, R.V., Morrison, S.M., Achilles, C.N., Ming, D.W., Vaniman, D.T., Blake, D.F., Tu, V.M., Chipera, S.J., Yen, A.S., Peretyazhko, T.S., Downs, R.T., Hazen, R.M., Treiman, A.H., Grotzinger, J.P., Castle, N., Craig, P.I., Des Marais, D.J., Thorpe, M.T., Walroth, R.C., Downs, G.W., Fraeman, A.A., Siebach, K. L., Gellert, R., Lafuente, B., McAdam, A.C., Meslin, P.Y., Sutter, B., Salvatore, M.R., 2020. Mineralogy of Vera Rubin Ridge from the Mars Science Laboratory CheMin Instrument. J. Geophys. Res.–planets 125 (9), e2019JE006306.

Ren, S., Zhou, X., Dai, T., Chu, Z., 1998. Laser Microprobe 40Ar/39Ar Isochron Dating of Alunite Ores from the Fanshan Deposit. Zhejiang Province. Chin. Sci. Bull. 13, 1443–1445.

Rudolph, W.W., Mason, R., 2001. Study of aqueous Al2(SO4)3 solution under hydrothermal conditions: sulfate ion pairing, hydrolysis, and formation of hydronium alunite. J. Solution Chem. 30 (6), 527–548.

Rye, R.O., 2005. A review of the stable–isotope geochemistry of sulfate minerals in selected igneous environments and related hydrothermal systems. Chem. Geol. 215 (1–4), 5–36.

Rye, R.O., Bethke, P.M., Wasserman, M.D., 1992. The stable isotope geochemistry of acid sulfate alteration. Econ. Geol. 87 (2), 225–262.

Sahlstrom, F., Chang, Z., Arribas, A., Dirks, P., Johnson, C.A., Huizenga, J.M., Corral, I., 2020. Reconstruction of an Early Permian, Sublacustrine Magmatic–Hydrothermal System: mount Carlton Epithermal Au–Ag–Cu Deposit. Northeastern Australia. Econ. Geol. 115 (1), 129–152.

Schauble, E., 2004. Applying stable isotope fractionation theory to new systems, in: Johnson, C.M., Beard, B.L., Albarède, F. (Eds.), Geochemistry of Non–Traditional Stable Isotopes. Mineralogical Society of America, Washington, D.C., pp. 65–111.

Smith, R.M., Martell, A.E., 1976. Critical Stability Constants, Vol. 4: Inorganic Complexes. Plenum Press, New York.

Stoffregen, R., 1993. Stability relations of jarosite and natrojarosite at 150–250–degrees–C. Geochim. Cosmochim. Acta 57 (11), 2417–2429.

Stoffregen, R., Alpers, C., Jambor, J., 2000. Alunite–jarosite crystallography, thermodynamics, and geochronology, in: Alpers, C.N., Jambor, J.L., Nordstrom, D.K. (Eds.), Sulfate Minerals: Crystallography, Geochemistry, and Environmental Significance. Mineralogical Society of America, Washington, D.C., pp. 453–479. DOI: 10.2138/rmg.2000.40.9.

Stoffregen, R.E., Cygan, G.L., 1990. An experimental–study of Na–K exchange between alunite and aqueous sulfate–solutions. Am. Mineral. 75 (1–2), 209–220.

Stoffregen, R.E., Rye, R.O., Wasserman, M.D., 1994a. Experimental studies of alunite.1. O–18–O–16 and D-H fractionation factors between alunite and water at 250–450–degrees–C. Geochim. Cosmochim. Acta 58 (2), 903–916.

Stoffregen, R.E., Rye, R.O., Wasserman, M.D., 1994b. Experimental studies of alunite.2. rates of alunite–water alkali and isotope–exchange. Geochim. Cosmochim. Acta 58 (2), 917–929.

Sun, Y., Xie, G., Chen, J., 2023. Alunite spectral features and mineral chemistry of the Zijinshan–Dafanshan lithocap in SE China: implications for mineral exploration. Acta Geochim. 42 (4), 585–602.

Tang, M., 2008. Study on Geological Characteristics and Ore Genesis of Da Fanshan Alunite Deposit in Luzong Basin, Anhui. Master's dissertation, Hefei University of Technology, Hefei, China.

Teng, F.-Z., Hu, Y., Ma, J.-L., Wei, G.-J., Rudnick, R.L., 2020. Potassium isotope fractionation during continental weathering and implications for global K isotopic balance. Geochim. Cosmochim. Acta 278, 261–271. https://doi.org/10.1016/j.gca.2020.02.029.

Wagman, D.D., et al., 1982. The NBS tables of chemical thermodynamic properties. J. Phys. Chem. Ref. Data 11 (Suppl. 2), 1–392.

Wang, K., Close, H., Tuller-Ross, B., Chen, H., 2020. Global Average Potassium Isotope Composition of Modern Seawater. ACS Earth Space Chem. 4 (7), 1010–1017. https://doi.org/10.1021/acsearthspacechem.0c00047.

Wang, F., Lan, X., Liang, X., 1997. A Preliminary Analysis of the Petrological Characteristics and Genesis of the Alunite Deposit in Pingyang. Zhejiang Geol. 01, 55–63.

Wang, T., She, J., Yin, K., Wang, K., Zhang, Y., Lu, X., Liu, X., Li, W., 2021. Sn(II) chloride speciation and equilibrium Sn isotope fractionation under hydrothermal conditions: a first principles study. Geochim. Cosmochim. Acta 300, 25–43.

Xia, Z., Lin, Y., Li, D., Reuning, L., Hu, Z., Liu, C., Mu, J., Li, W., 2024. Equilibrium Mg and K isotope fractionation between carnallite and saturated brine: calibrations and applications. Geochim. Cosmochim. Acta 371, 173–188.

Zeng, H., Rozsa, V.F., Nie, N.X., Zhang, Z., Tuan Anh, P., Galli, G., Dauphas, N., 2019. Ab Initio Calculation of Equilibrium Isotopic Fractionations of Potassium and Rubidium in Minerals and Water. ACS Earth Space Chem. 3 (11), 2601–2612.

Zhang, L., 2011. Study on Petrogenetic and Metallogenic Processes in the Luzong Basin, Anhui Province. Ph.D. dissertation, Hefei University of Technology, Hefei, China.

Zheng, X.-Y., Beard, B.L., Neuman, M., Fahnestock, M.F., Bryce, J.G., Johnson, C.M., 2022. Stable potassium (K) isotope characteristics at mid–ocean ridge hydrothermal vents and its implications for the global K cycle. Earth Planet. Sci. Lett. 593, 117653.

Zhou, Y., Fan, F., Xing, G., Zhang, H., Xiu, L., Chen, S., Xu, M., Li, L., Yang, K., Chen, J., 2022. Characteristics and genesis of the Fanshan lithocap, Zhejiang Province: exploration implications from the largest alunite deposit of China. Ore Geol. Rev. 149, 105038.